Application of adjoint-based optimization in three-dimensional flows interacting with multiple moving bodies

by

Daniel Colgan

B.S., Bucknell University, 2013

M.S., Missouri University of Science and Technology, 2020

A THESIS

submitted in partial fulfillment of the
requirements for the degree

MASTER OF SCIENCE

Alan Levin Department of Mechanical and Nuclear Engineering
Carl R. Ice College of Engineering

KANSAS STATE UNIVERSITY
Manhattan, Kansas

2023

Approved by:

Major Professor
Mingjun Wei

Copyright

Abstract

Throughout nature, bodies in motion rarely move independent of each other but are often not studied in this multiple body form. This is often due to the complex motion exhibited by these bodies such as flocks of birds, pods of whales, or schools of fish. However, on a more fundamental level, the control space required to study any of these multiple body cases is immense and computationally unfeasible using traditional approaches. The continuous adjoint-based approach applied to a three-dimensional, multiple body case allows for a computationally feasible approach to study the complex flow-structure interactions for optimization and physical understanding. The computational cost associated with an adjoint-based approach is independent of the number of control parameters, making it an ideal method to solve complex problems with large control space.

The traditional formulation of the adjoint equations utilize a fluid domain with fixed solid boundaries. However, with the introduction of moving solid boundaries, inconsistencies and ambiguity arise from the interaction between the Eulerian fluid domain and Lagrangian solid boundary when perturbation is considered at the solid boundary. Traditional methods utilize an unstable mapping function to mitigate the challenges of a moving boundary but increase the computational cost drastically and tend to be too complex to feasibly derive. To bypass the complexity required to use an unstable mapping function, application of non-cylindrical calculus allows for the simplification of the mapped domain to only the moving solid boundary. This approach, validated previously by the research group, is applied to study the broadening of the approach to encompass multiple bodies in a three-dimensional fluid flow and inherent challenges in implementation.

The adjoint-based approach is first applied to optimize the motion of a pair of spheroids in an echelon formation to identify lift-generating regions behind a heaving leading body. The echelon pair case also explores the effect of variations in size of the trailing body. The lift-generation results identify a region directly behind a diving leading body and external

vortex wall that can attribute over a relative 500% increase in force. Future work applies the approach to successively and collectively to optimize a formation of spheroids and identify challenges in application to optimization of several bodies simultaneously.

Table of Contents

List of Figures

List of Tables

Nomenclature

A	=	area of the solid body
C_D	=	coefficient of drag
D	=	spanwise diameter
$g(\phi)$	=	gradient function
$\mathcal{J}$	=	cost function
$\mathcal{N}(\boldsymbol{q})$	=	operator for Navier-Stokes equations
$\mathcal{N}^*(\boldsymbol{q})\boldsymbol{q}^*$	=	operator for adjoint equations
$\boldsymbol{n}$	=	normal direction
p	=	pressure
$\boldsymbol{q}$	=	flow/primary variable that contains $[p, \boldsymbol{u}]^T$
$\bar{r}$	=	Cartesian coordinate array that contains $[x, y, z]$
Re	=	Reynolds number
$\mathcal{S}$	=	solid boundary
T	=	period of oscillatory behavior
t	=	dimensional simulation time
$\boldsymbol{U}$	=	incoming flow velocity
$\boldsymbol{u}$	=	velocity
$\boldsymbol{V}$	=	velocity at solid boundary
Z	=	derivative of boundary location with respect to control parameters (Lagrangian)
Γ_∞	=	far field boundary
Δt	=	time step for direct simulation and adjoint-based optimization
δ_{ij}	=	Kronecker delta
ν	=	kinetic viscosity
ρ	=	density of solid body
σ_{ij}	=	stress tensor
ϕ_m	=	control parameter of solid body m
ϕ_A	=	amplitude of control parameter
ϕ_θ	=	phase of control parameter
Ω	=	fluid domain
ω	=	vorticity
Superscripts		
$'$	=	derivative in Eulerian space
$\cdot$	=	derivative in Lagrangian space
$*$	=	adjoint variables or operator

Acknowledgments

First and foremost, I want to express my gratitude to my advisor, Prof. Mingjun Wei, for his continuous support and mentorship through my brief time at Kansas State University. Through his guidance and knowledge in computational methods, Dr. Wei enabled me to freely pursue various phenomenon found in nature and advance the work of the Computational Science for Fluids and Acoustics Lab. His insights and enthusiasm for learning has been contagious and will remain with me as I transition back to military life and in future academic endeavors. I am honored to have been one of his graduate students.

I also want to express my appreciation to Prof. Shin-Kang Fan and Prof. Raj Kumar Pal for serving as my committee members for their encouragement, comments, and provoking discussions.

To my fellow graduate students, Jon Grote and Veeshal Modi, I want to thank you for your friendship and support through the long hours fighting through problem sets. To my fellow lab mates, Bolun Xu and Sherif Elsayed, thank you for your comments and guidance in the past year. Without your expertise, the learning curve for computational research would have been much more daunting. Additionally, I would be remiss to not thank the foundational work completed by Dr. Xu in establishing the current structure of the numerical simulation and adjoint-based optimization modules.

Furthermore, I gratefully acknowledge the financial and professional support of the U.S. Army Advanced Civil Schooling program and the United States Military Academy Department of Mathematical Sciences.

Last of all, I would like to thank my family for their continued selfless support and encouragement to be a lifelong learner. I would also like to immortalize my furry friends, Anabella and Lilian, who have kept me grounded and sane through the years. Finally, to my wife who has supported me through all the trials and tribulations of life, this would not of been possible without you.

Dedication

To my parents, my brothers,

and my wife.

Chapter 1

Introduction

Throughout nature, co-dependent animals move together in coordinated patterns and formations for safety and protection within the group but also to take advantage of fluid dynamic interactions when pertaining to flight and aquatic motion. These interactions can range from drafting effects to generation of propulsive forces. However, multiple body motion is a very complex and computationally costly problem to study. Due to the size of the domain and large control space required, the computational exploration of multiple body systems cannot feasibly be studied using traditional approaches. In the following sections, the motivational sources for the current work will be explored in detail along with various optimization techniques and the progression on the current adjoint optimization method.

1.1 Multiple Bodies in Motion in Nature

Various aquatic animal species have adapted over millions of years to group together for social protection and beneficial hydrodynamic interactions and remains and intriguing subject of study for engineers. Study of individual motion and articulation has been and continues to be researched for understanding[1;2] and applied from an engineering perspective in biomimicry applications.[3] With the continued advancements in technology, the computational resources available to researchers also continues to grow. Where initial research focused on

an individual specimen and its specific interactions with the natural world, research has expanded into the study of interactions between individuals and collective behaviors.[4]. For this work, motivation is taken from two sources found in nature: whales traveling in echelon formations and structured formations of fish schools.

1.1.1 Echelon Pattern Formation: Whale Pods

With whales appearing in every ocean in the world, the biological impact of these creatures cannot be understated. As a result, the behavior of whales and whale pods continues to be a topic of observational research from the perspective of biology.[5–10] From an engineering perspective, study of whales tend to focus on general individual undulating motion and specific aspects of interaction with the fluid flows such as bio-mimicry passive flow control mechanics.[6;11] Therefore, the interactions between whales in close proximity remains to be explored further. Initial and continuing research into echelon formation delves into the effect of undulation for vortex harvesting[12;13] and Bernoulli suction effect in dolphin drafting.[14] However, the behavior observed in mother-calf interactions[5;8–10] over long distance migrations remains relatively computationally unexplored. This behavior is the inspirational source for Chapter 3 as the interactions between a leading and trailing body of various sizes are explored to identify lift generating behaviors in fluid structure interactions.

1.1.2 Diamond Pattern Formations: Fish School

Unlike whale pod formations, fish schooling exhibits a much more alluring draw for academic pursuit from multiple disciplines. One aspect of fish schooling that is heavily studies is the social interaction between independent elements that lead to the development of school formations.[15–19] However, studies into the social interactions tend to utilize a simplification or omission of vortex shedding patterns and do not provide insight into the fluid structure interactions within the school. Forays into fluid dynamic interactions have, until the past decade, have been limited to two-dimensional cases of fixed formations[20–23] or experimental studies into two swimmer setups that explore the undulating motion of various species of

fish.[12;24] Like the social interaction studies, the two-dimensional cases, although beneficial in understanding, also make assumptions within the flow that simplify the problem and create a skewed understanding of the interactions occurring. With increases to computing power, study in three-dimensions is becoming more available outside of utilizing super-computing. Recently, research has begun to delve into the three-dimensional and optimization aspect of formations but uses traditional parametric studies and undulating motion from specific species.[13;25] With the application of adjoint-based optimization, as demonstrated in this research, further exploration into fluid structure interactions and optimization of formations is possible with a computationally feasible method.

1.2 Optimization for Motion

Optimization of a formation of solid bodies involves numerous control parameters to adequately account for complex motion, deformation, and positioning. Due to the resulting size of the required control space, a traditional parametric case becomes computationally impossible. Due to its inherent properties, an adjoint approach is an ideal gradient-based method to apply to a large control space. The adjoint approach is able to calculate the gradient simultaneously for an arbitrary number of control parameters with a single computation in a formulated adjoint domain. This reduces the computational cost immensely as the total cost to calculate the sensitivity of the cost function is independent of the total number of control parameters. This approach has been thoroughly implemented in the study of a flapping wing and serves as the foundation for this research.[26–30]

1.3 Current Work

The original applications of the adjoint-based optimization approach include airfoil shape optimization[31], turbulence control[32], and jet noise control.[33] Recently, this approach evolved through the use of non-cylindrical calculus to address problems with moving solid boundaries.[28] These new capabilities were subsequently applied to two and three-dimensional flap-

ping wings[26;27] and a deforming three-dimensional wing.[30] The logical progression is to then apply the adjoint-based optimization approach to a multi body system. The existing computational code evaluated single body movement in three-dimensions with the ability to implement deformation into rigid bodies. This study expands the accessible control parameters to include positional changes for optimization and introduces and implements the required coding to control and optimize multiple bodies in the same flow. Therefore, the goal of this research is to progressively apply the adjoint approach to an increasingly complex systems to explore various natural phenomena and determine viability of the approach in a multiple body environment. Exploration of an echelon pair formation identifies regions in the leading body's wake for generating lifting forces along with exploring the effect of variations in size in the resulting optimization. With the viability of the approach determined in the echelon pair formation study, future work will apply the adjoint approach to a diamond pattern formation classically studied in two-dimensions while looking at drag reduction within the entire system of bodies.

The subsequent thesis is organized in the following structure. The formulation of the governing and adjoint equations, implemented concepts, non-cylindrical calculus derivation, and numerical implementation are detailed in Chapter 2. The application of the adjoint-based optimization method is then applied to the echelon pair formation in Chapter 3. Final conclusion on the complete work are outlined in Chapter 4.

Chapter 2

Theoretical Formulation and Numerical Implementation

The formulation of the continuous adjoint equations utilized in this study build upon the fixed domain derivation by Wei and Freund[33] and the subsequent adaptation to moving boundary conditions within a morphing domain utilizing non-cylindrical calculus by Xu and Wei[28] This work applies these concepts to three-dimensional, multi-body incompressible, viscous Navier-Stokes governed flows.[34] The following chapter outlines the governing equations and theories that are implemented into the numerical algorithms and conditions that are used to formulate direct numerical simulation solutions to three-dimensional, multi-body flows.[27;35;36]

2.1 Foundational Formulation and Theory

The following formulation relies on non-dimensionality to reduce computational costs associated with material property interactions and prescribed solid motion that allows for the flow field to be determined by the Navier-Stokes equations and solid boundary velocity for velocity mapping. Therefore, the direct numerical simulation generated and optimized flow structures utilize a prescribed solid motion that is discussed in subsequent chapters in conjunction with specific implementations and implements the following derivation.

2.1.1 Governing Equations

For the implementation discussed in this work, the flow is governed by the incompressible Navier-Stokes equations in a fluid domain, Ω, and prescribed incoming velocity, $V(t)$,

$$\begin{aligned} \nabla \cdot \boldsymbol{u} &= 0 \\ \tfrac{\partial \boldsymbol{u}}{\partial t} + (\boldsymbol{u} \cdot \nabla)\boldsymbol{u} &= -\nabla p + \tfrac{1}{Re}\nabla^2 \boldsymbol{u} \end{aligned} \tag{2.1}$$

with the following solid boundary conditions,

$$\begin{aligned} \boldsymbol{u} &= \boldsymbol{V} \quad \text{on} \quad \mathcal{S}, \\ \boldsymbol{u} &= \boldsymbol{U} \quad \text{on} \quad \Gamma_\infty, \\ \tfrac{\delta p}{\delta n} &= 0 \quad \text{on} \quad \Gamma_\infty \end{aligned} \tag{2.2}$$

where $\mathcal{S}$ and Γ_∞ are respectively the solid boundary and the far-field boundary; n denotes the unit normal vector at Γ_∞; $\boldsymbol{u}$ is the velocity vector containing $[u, v, w]$;and the respective boundary velocity vectors are $\boldsymbol{U}$ and $\boldsymbol{V}$. Eqn. 2.1 can be written operator form, $\mathcal{N} = 0$, with the flow variable defined as $\boldsymbol{q} = [p \;\; \boldsymbol{u}]^T$ where $\boldsymbol{p}$ is pressure,

$$\mathcal{N}(\boldsymbol{q}) = \begin{bmatrix} \frac{\partial u_j}{\partial x_j} \\ \frac{\partial u_i}{\partial t} + \frac{\partial u_j u_i}{\partial x_j} - \frac{\partial^2 u_i}{\partial x_j^2} + \frac{\partial p}{\partial x_i} \end{bmatrix} = 0 \tag{2.3}$$

This operator is later used in the derivation of the adjoint method for simplification purposes.

2.1.2 Immersed Boundary Method

To alleviate computationally expensive re-meshing of conformal grids in the numerical implementation of the derivation, the immersed boundary method developed originally by Peskin[37] and later adapted by others[38–43] is introduced and implemented. The immersed boundary method has become a popular method for simulating complex flow-structure interactions with many variations and refinements since its first development. The method utilizes a fixed Eulerian grid for the fluid flow and a moving Lagrangian grid for the solid boundary or immersed boundary as shown in Fig.2.1 and couples the grids with a forcing term applied

continuously or discretely to the governing equations.

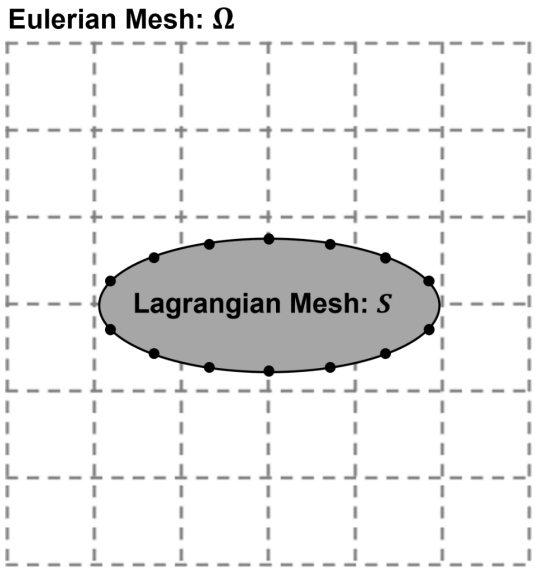

Figure 2.1: Diagram of the Eulerian/Lagrangian mesh utilized by the immersed boundary method. The fluid domain, Ω, utilizes a fixed Eulerian mesh. The boundary of the solid body, $\mathcal{S}$, utilizes a Lagrangian mesh. The interaction of the intersection of the two meshes is captured by the immersed boundary method.

The original implementation by this work was influenced by immersed boundary concepts adapted by Fadlun et al.[42] Therefore, a discrete forcing function is used to enforce solid boundary conditions and is applied to both forward (fluid flow) and backward (adjoint) simulations. This allows for the implication that $\boldsymbol{u}$ on the boundary is different than $\boldsymbol{V}$ such that the forcing function, $\boldsymbol{f}$, rectifies the difference.[42] With the implementation of the immersed boundary method discrete forcing function, Eqn.2.1 becomes the following,

$$\frac{\partial \boldsymbol{u}}{\partial t} + (\boldsymbol{u} \cdot \nabla)\boldsymbol{u} = -\nabla p + \frac{1}{Re}\nabla^2 \boldsymbol{u} + \boldsymbol{f}, \tag{2.4}$$

where the forcing term is defined as,

$$\boldsymbol{f} = \begin{cases} [(\boldsymbol{u} \cdot \nabla)\boldsymbol{u} - \frac{1}{Re}\nabla^2 \boldsymbol{u}]^n + \frac{1}{\Delta t}(\boldsymbol{V} - \boldsymbol{u}^n), & \text{in} \quad \mathcal{S} \\ 0, & \text{otherwise,} \end{cases} \tag{2.5}$$

In the immersed boundary formulation, n denotes the n-th time step of the discretization

where Δt is the associated time step. With the addition of additional bodies into the fluid flow, each solid body, m, is controlled by some control parameter, $\boldsymbol{\phi}_m$, such that the corresponding solid boundary, $\mathcal{S}_m$, and velocity fields, $\boldsymbol{V}m$, are defied as $\mathcal{S}_{m,i} = \mathcal{S}_{m,i}(\phi_m, t)$ and $\boldsymbol{V}_{m,i} = \boldsymbol{V}_{m,i}(\phi_m, t)$.

2.1.3 Cost Function

In order to optimize and evaluate the fluid-structure interactions and vortex structures, the cost function for force, $\mathcal{J}$, is formulated to evaluate the forces acting on the solid bodies as in any given direction in accordance with the Kronecker delta as,

$$\mathcal{J} = \frac{1}{TD_0} \int_T \int_{\mathcal{S}} \sigma_{ij} n_j ds dt, \tag{2.6}$$

where T is the period of oscillation; $D_0 = U^2 A/2$ where A is the area of the spheroid; and the stress is defined as,

$$\sigma_{ij} = -\frac{p}{\rho}\delta_{ij} + \nu \left(\frac{\partial u_i}{\partial x_j} + \frac{\partial u_j}{\partial x_j} \right) \tag{2.7}$$

where ρ and ν are equal to one to maintain non-dimensionality. The utilization of the Kronecker delta allows for specific cost functions associated to cartesian directions. For example, σ_{1j} would denote forces acting in the x-direction where σ_{2j} and σ_{3j} would denote forces in the y-direction and z-direction respectfully. In this work, we focus on lift forces associated in the z-direction. Thus, with the cost function, $\mathcal{J}$, defined, the sensitivity to any control, $\boldsymbol{\phi}$, can be computed by the perturbed function, $\mathcal{J}'$, under an arbitrary perturbation, $\boldsymbol{\phi}'$, which is defined by the Fréchet differential,

$$\mathcal{J}' \equiv \lim_{\varepsilon \to 0} \frac{\mathcal{J}(\boldsymbol{\phi} + \varepsilon \boldsymbol{\phi}') - \mathcal{J}(\boldsymbol{\phi})}{\varepsilon} \tag{2.8}$$

Thus when optimizing the cost function, the sensitivity analysis from Eqn. 2.8 informs the gradient, $g(\boldsymbol{\phi})$, such that the control variables are iteratively update with a relaxation factor, α, by,

$$\boldsymbol{\phi}^{NEW} = \boldsymbol{\phi}^{OLD} - \alpha g(\boldsymbol{\phi}) \tag{2.9}$$

However, it is usually hard or impossible to directly compute the gradient function, $g(\phi)$, when more than one control parameter exists in the problem.

2.2 Adjoint Formulation and Theory

Adjoint-based methods provide a unique way to compute the gradient function using a combination of flow and adjoint variables. Most importantly, the computational cost of adjoint-based method does not scale up with the increased control parameters. Thus, it becomes the only feasible approach in dealing with various problems with a large control space. However, due to the implementation of the immersed boundary method, traditional adjoint methods are not viable for optimization of moving boundaries. Therefore, non-cylindrical calculus is used to couple the fluid flow (Eulerian) and the moving boundary (Lagrangian) frameworks in order to maintain a continuous adjoint formulation.[44;45]

Before proceeding into the application of the non-cylindrical calculus, it is important to reestablish the frameworks defined previously to remain consistent with the governing equations in Eqn.2.1 and establish the need to couple the frameworks. All analysis is naturally conducted in the Eulerian framework and contains the governing equations for the fluid flow to include the derivatives and gradient equations. The application of dynamics and kinematics along the moving boundary often requires variables to be defined in a Lagrangian framework.

It is possible to use an unsteady mapping function to map the entire fluid domain to a fixed computational domain. However, the complexity of the derivation and formulation makes it unfeasible for practical uses.[45] The non-cylindrical calculus method only focuses on mapping the change to the domain boundaries, greatly reducing the complexity, and making it the practical choice for use.[46] Protas and Liao[45] proposed a new adjoint-based approach using non-cylindrical calculus for mapping that was further developed by Xu and Wei[33] that provides the possibility to use a adjoint-based strategy for the optimization of structure motion or morphing in a fluid flow domain as shown in Fig. 2.2.

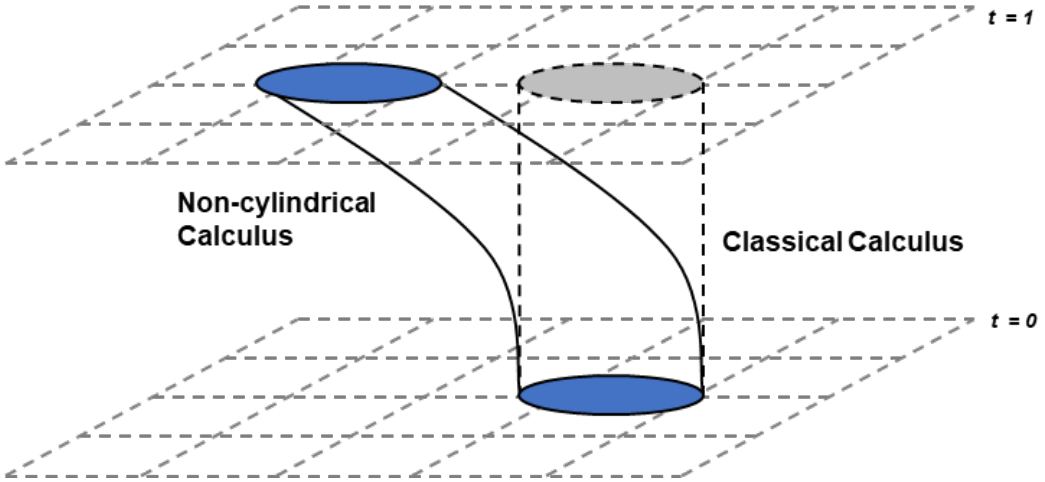

Figure 2.2: Diagram of non-cylindrical calculus in a morphing domain versus classical calculus in a fixed domain. Here, non-cylindrical calculus is applied to a boundary morphing in time whereas classical calculus is cylindrical for a boundary fixed in time.

2.2.1 Non-Cylindrical Calculus

To begin the the application of the non-cylindrical calculus, the flow map, $\mathcal{T}(t, \tau, \phi)$ and transverse flow map, $\bar{\mathcal{T}}(t, \varepsilon, \phi)$, are defined for the fluid domain, Ω, and the control, ϕ, respectfully as

$$\mathcal{T}(t, \tau, \phi) : \Omega(t, \phi) \to \Omega(t + \tau, \phi) \tag{2.10}$$

$$\bar{\mathcal{T}}(t, \varepsilon, \phi) : \Omega(t, \phi) \to \Omega(t, \phi + \varepsilon\phi') \tag{2.11}$$

which requires a boundary-to-boundary mapping. Similarly, the velocity flow maps, $\mathbb{V}$ and transverse $\mathbb{Z}$, are defined by taking the derivative with respect to the local time variance, τ, and the perturbed control parameter step, ε,

$$\mathbb{V}(t, \tau, \boldsymbol{x}) = \left.\frac{\partial \mathcal{T}(t, \tau, \phi, \boldsymbol{x})}{\partial \tau}\right|_{\tau=0} \tag{2.12}$$

$$\mathbb{Z}(t, \tau, \boldsymbol{x}) = \left.\frac{\partial \bar{\mathcal{T}}(t, \varepsilon, \phi, \boldsymbol{x})}{\partial \varepsilon}\right|_{\varepsilon=0} \tag{2.13}$$

Here, a new boundary condition is established such that the flow map velocity is equal to the physical velocity on the solid boundary, $\mathcal{S}$,

$$\mathbb{V}(t,\phi,\boldsymbol{x}) = \boldsymbol{V}(t,\phi,s) \quad \text{on} \quad \mathcal{S} \tag{2.14}$$

To delineate between the Eulerian and Lagrangian frameworks for any given function f, a derivative in a Lagrangian framework uses the notation $\dot{f}$ where as a derivative in an Eulerian framework uses the notation f'. Therefore, a non-cylindrical material derivative, $\dot{f}$ is defined as

$$\dot{f}(t,\boldsymbol{x}) \equiv \lim_{\varepsilon\to 0} \frac{f(t,\phi+\varepsilon\phi',\bar{\mathcal{T}}(t,\varepsilon,\phi,\boldsymbol{x})) - f(t,\phi,\boldsymbol{x})}{\varepsilon} \tag{2.15}$$

where $\dot{f}$ is related to the non-cylindrical shape derivative, f' by

$$f' = \dot{f} - \mathbb{Z}\cdot\nabla f \tag{2.16}$$

Through the non-cylindrical material derivative, the flow map velocity and transverse velocity can also be related associated

$$\dot{\mathbb{V}} = \frac{d\mathbb{Z}}{dt} \tag{2.17}$$

2.2.2 Linear Perturbation Equation

With the shape derivatives defined, they can now be applied to the Navier-Stokes equations, Eqn. 2.1, to derive the new linear perturbation equations

$$\begin{aligned}
\mathcal{N}'(\boldsymbol{q})\boldsymbol{q}' &= 0 \quad \text{in} \quad \Omega,\\
\boldsymbol{u}' = \dot{\mathbb{V}} - \mathbb{Z}\cdot\nabla\boldsymbol{u} &\quad \text{on} \quad \mathcal{S},\\
\boldsymbol{u}'|_{t=0} &= 0 \quad \text{in} \quad \Omega,\\
\dot{\mathbb{V}} = \tfrac{d\mathbb{Z}}{dt} &\quad \text{on} \quad \Gamma_\infty,\\
\mathbb{Z}|_{t=0} &= 0 \quad \text{on} \quad \Gamma_\infty
\end{aligned} \tag{2.18}$$

where

$$\mathcal{N}'(\boldsymbol{q})\boldsymbol{q}' = \begin{bmatrix} \frac{\partial u_j'}{\partial x_j} \\ \frac{\partial u_i'}{\partial t} + \frac{\partial u_j' u_i}{\partial x_j} + \frac{\partial u_j u_i'}{\partial x_j} - \frac{\partial^2 u_i'}{\partial x_j^2} + \frac{\partial p'}{\partial x_i} \end{bmatrix} \tag{2.19}$$

Similar to the perturbation of the gradient, the flow variable, $\boldsymbol{q}$, is also defined by Fréchet differential such that,

$$\boldsymbol{q}'(t, \boldsymbol{\phi}, \boldsymbol{x}) \equiv \lim_{\varepsilon \to 0} \frac{\boldsymbol{q}(t, \boldsymbol{\phi} + \varepsilon \boldsymbol{\phi}', \boldsymbol{x}) - \boldsymbol{q}(t, \boldsymbol{\phi}), \boldsymbol{x}}{\varepsilon} \tag{2.20}$$

2.2.3 Adjoint Formulation

The formulation of the adjoint-based system of equations introduces the adjoint variables, $\boldsymbol{q}^* = [p^* \quad \boldsymbol{u}^*]^T$ and $\boldsymbol{Z}^*$, as Lagrange multipliers to impose the fluid flow equations and transverse mapping. The fluid flow equations and boundary conditions become

$$\begin{aligned} \mathcal{N}^*(\boldsymbol{q})\boldsymbol{q}^* = 0 \quad & \text{in} \quad \Omega, \\ \boldsymbol{u}^* = \boldsymbol{\delta}_{ij} \quad & \text{on} \quad \mathcal{S}, \\ \boldsymbol{u}^* = 0 \quad & \text{on} \quad \Gamma_\infty, \\ \tfrac{\delta p}{\delta n} = 0 \quad & \text{on} \quad \Gamma_\infty \end{aligned} \tag{2.21}$$

where

$$\mathcal{N}^*(\boldsymbol{q})\boldsymbol{q}^* = \begin{bmatrix} \frac{\partial u_j^*}{\partial x_j} \\ \frac{\partial u_i^*}{\partial t} + \boldsymbol{u}_j(\frac{\partial u_i^*}{\partial x_j} + \frac{\partial u_j^*}{\partial x_i}) + \frac{\partial^2 u_i^*}{\partial x_j^2} + \frac{\partial p^*}{\partial x_i} \end{bmatrix} \tag{2.22}$$

Therefore, applying the adjoint conditions to the cost function established in Eqn. 2.6, the gradient of the cost function with respect to the control parameter, ϕ, is

$$g_l = \frac{\partial \mathcal{J}}{\phi_l} = -\frac{1}{TD_0} \int_T \int_S \left[Z_{k,l} \frac{\partial \sigma_{ij}}{\partial x_j} n_k - Z_i^* (\frac{\partial V_i}{\partial \phi_l} - Z_{k,l} \frac{\partial u_i}{\partial x_k}) \right] dsdt \tag{2.23}$$

where

$$Z_{i,j} = \tfrac{\partial \mathcal{S}_i}{\partial \phi_l}, \qquad Z_i^* = \sigma_{ij}^* n_j + u_j^* u_j n_i \tag{2.24}$$

With this formulation, gradient updates to the control parameter move towards a decrease in the cost function during optimization. For a complete, in depth derivation, refer to the details within the original work by Xu and Wei.[28] Since the formulation of the adjoint and gradient equations is derived through a continuous approach, they are independent of the numerical implementation. Thus, the gradient for optimization can be computed once the forward (physical flow) and backwards (adjoint) equations are solved once where the computational cost of the two runs is comparable.

2.3 Numerical Implementation

The computational domain utilizes a staggered Cartesian mesh with local refinement through stretching functions for numerical efficiency and numerical stability.[34;38;47] A second-order central difference is implemented for spatial discretization with a second-order Adams-Bashforth/Crank-Nicholson scheme used for time advancement. A Fast Fourier transform (FFT) with a generalized cyclic reduction algorithm is used to solve the pressure Poisson equation while a projection method for incompressible flow conditions is implemented. The Courant-Friedrichs-Lewy (CFL) constraint,

$$CFL = \Delta t \max(\frac{|u_i|}{\Delta x_i}) \leq \sqrt{3} \tag{2.25}$$

limits the time step for a third-order Runge-Kutta scheme. Once the gradient is calculated, a Polak-Ribiere variant of the conjugate gradient method is used to update the main iterations.

Due to the considerations for nonlinear constraints are considered, the NLopt free/open-source library is used to update the control parameter in sub-iterations. The NLopt library is called directly with built in Fortran APIs by the in-house Fortran simulation code. The NLopt library utilizes an internal line search method and is implemented to utilize a combined optimization by linear approximation (COBYLA) scheme. This scheme builds successive linear approximations of the cost function and imposed constraints via a simplex of $n+1$ points in n dimensions that are optimized in a trust region for each time step.[48] For

the sub-iterations, the optimal time step is calculated by the NLopt library. The software requires between five and eight sub-iterations and three to five main iterations for convergence depending on the number of control parameters and the associated error tolerances.

The Fortran code developed for this work ran on multi-core computer servers in the Computational Science for Fluids and Acoustics (C-SOFA) Lab at Kansas State University. The servers utilize Intel Xeon E5 processors operating at 2.4 GHz with a Linux operating system. Computational runs utilize a Message Passing Interface (MPI) configuration to access ten to twenty of the twenty-eight available core for three-dimensional simulations. Due to system configurations and hardware limitations, the scope of the complexity of multi-body simulations is limited by computational resources and downlink speeds for data files.

Chapter 3

Optimization of Echelon Pair

Taking inspiration from observed mother-calf behavior observed in nature[9;10], this chapter explores the regions behind a heaving body that are available for generating lift by a trailing or following body in a multiple moving body flow. The trailing body is optimized over five active controls using the adjoint-based approach discussed in Chapter 2 to maximize the coefficient of lift over one period of oscillation. The effect of variations in the size of the trailing body is explored to further determine interactions between the bodies. Through this case study, the challenges and limitations in the application of the adjoint-based optimization approach are identified and discussed.

3.1 Kinematic Setup and Initial Conditions

Fig. 3.1 (a-b) shows the kinematic and motion decomposition parameters for the echelon pair formation in this study. The solid bodies adhere to a $5:1$ length to diameter ratio with the leading body as the reference body for spacing calculations. The size of the trailing body is varied in relation to the leading body in the respective following sections at 100%, 75%, 50%, and 25%.

Both bodies exhibit heaving motions as shown by the control parameters in Fig. 3.1 (b) where only the trailing body motion and position is actively controlled during optimization

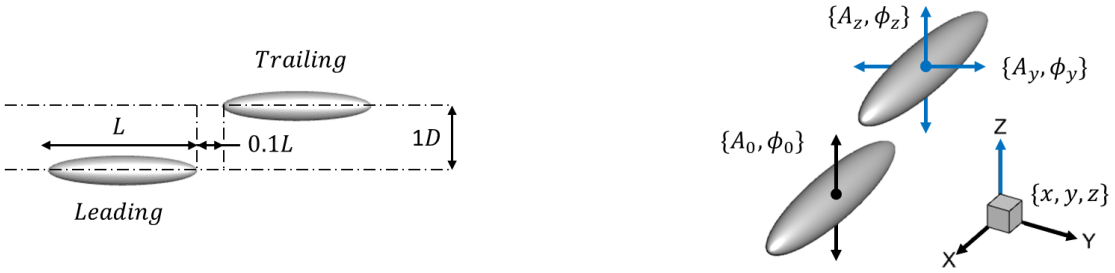

(a) (b)

Figure 3.1: Kinematic setup and motion decomposition. a) Schematic of the spatial positioning and layout for the study of the echelon pair formation. b) Schematic of the decomposition of motion and active (——) and fixed (——) control parameters.

in this case study. The motion equations are

$$\begin{aligned} z(\phi_z, t) &= A_z \sin(2\pi f t + \theta_z), \quad & \phi_z &= A_z, \theta_z \\ y(\phi_y, t) &= A_y \sin(2\pi f t + \theta_y), \quad & \phi_y &= A_y, \theta_y \\ R(\bar{r}, t) &= R(t) + \bar{r}, & \bar{r} &= (x, y, z) \end{aligned} \tag{3.1}$$

Here, $\bar{r}$ is the position vector containing the cartesian location of the solid body. Due to the magnitude of the gradient in the x and y-direction, these position controls are fixed with the position in the z-direction bounded by $\pm D$. The amplitudes of the heaving motions are also bounded by $\pm D$. With the prescribed bounded box, it is important to note that this study does not look at the efficiency of the trailing body while maximizing lifting forces. Finally, the Reynolds number utilized for this study is set at 200 for computational efficiency in exploring the applicability of the adjoint-based optimization approach.

Four time periods for initial condition fluid-structure interactions are documented in Fig. 3.3, along with the tabulated values for control parameter values in Table 3.1. The initial conditions establish the following body outside of the wake of the leading body in a region of unperturbed flow. Initial movement conditions force the trailing body into the lead body's wake and subsequently optimized from this interaction. The cost function for the echelon

Table 3.1: Initial and optimized values for the evaluated degrees of freedom of the trailing body in the echelon pair formation at $Re = 200$. The initial condition for the x-location, denoted as " ", varies by the prescribed value as dictated in the kinematic setup.

Simulation	$[A_y, \theta_y]$	$[A_z, \theta_z]$	$[x, y, z]$	$C_{L,0}$	C_L
IC:Lead	[0, 0]	[0.5, 0]	[0, 0, 0]	*	*
IC:Follow	[0.25, 0]	[0.1, 0]	[, 0.5, 0]	*	*
OPT:100%	[0.42, 1.13]	[0.5, -0.67]	[1.0, 0.5, -0.5]	0.00243	0.02188
OPT:75%	[0.5, 0.126]	[-0.5, -0.179]	[0.9375, 0.5, -0.5]	0.00162	0.01260
OPT:50%	[-0.037, 0.024]	[-0.188, -0.266]	[0.625, 0.5, -0.5]	0.00046	0.00279
OPT:25%	[-0.107, 0.394]	[-0.081, -0.768]	[0.3125, 0.5, -0.5]	0.00003	0.00096

pair formation only considers the z-force generated by the trailing body under active control.

3.2 Evaluation of Fluid-Structure Interactions.

In order to visualize the fluid-structure interaction, an iso-surface of a positive Q criterion with an overlay of the vorticity magnitude, $||\omega||$. The Q criterion is derived based on the second invariant of the velocity gradient tensor. The velocity gradient, $\nabla \boldsymbol{v}$, can be simplified into the following two parts: a symmetric part or the rate of strain, $\boldsymbol{S}$, and a anti-symmetric part or vorticity tensor, Ω, derived as

$$\nabla \boldsymbol{v} = \frac{1}{2}(\nabla \boldsymbol{v} + \nabla \boldsymbol{v}_T) - \frac{1}{2}(\nabla \boldsymbol{v} - \nabla \boldsymbol{v}^T) = \boldsymbol{S} + \boldsymbol{\Omega} \tag{3.2}$$

The Q criterion is then derived as

$$Q = \frac{1}{2}(||\boldsymbol{\Omega}||^2 - ||\boldsymbol{S}||^2) \tag{3.3}$$

By this definition, areas dominated by vorticity occur where $Q > 0$.[49]

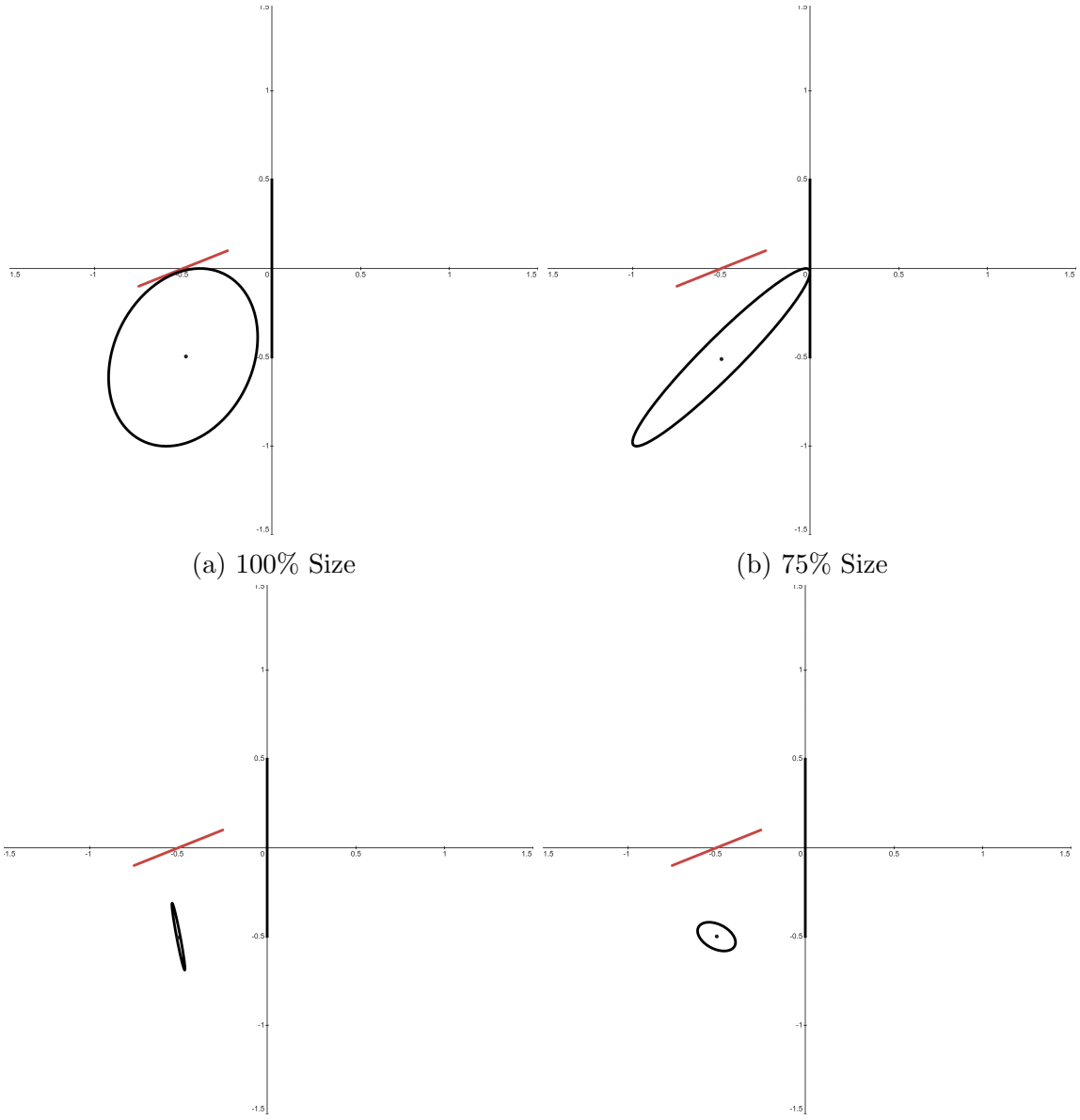

(a) 100% Size

(b) 75% Size

(c) 50% Size

(d) 25% Size

Figure 3.2: Trajectory Path for Optimized Values. Transcribed trajectories of optimized values found in Table 3.1 of both optimized trajectory (———) and initial trajectory (———. The trajectory of the leading body on the right is not actively controlled and therefore unchanged. All optimized paths travel in a clockwise direction in current depictions. The optimized center position is denoted as "•".

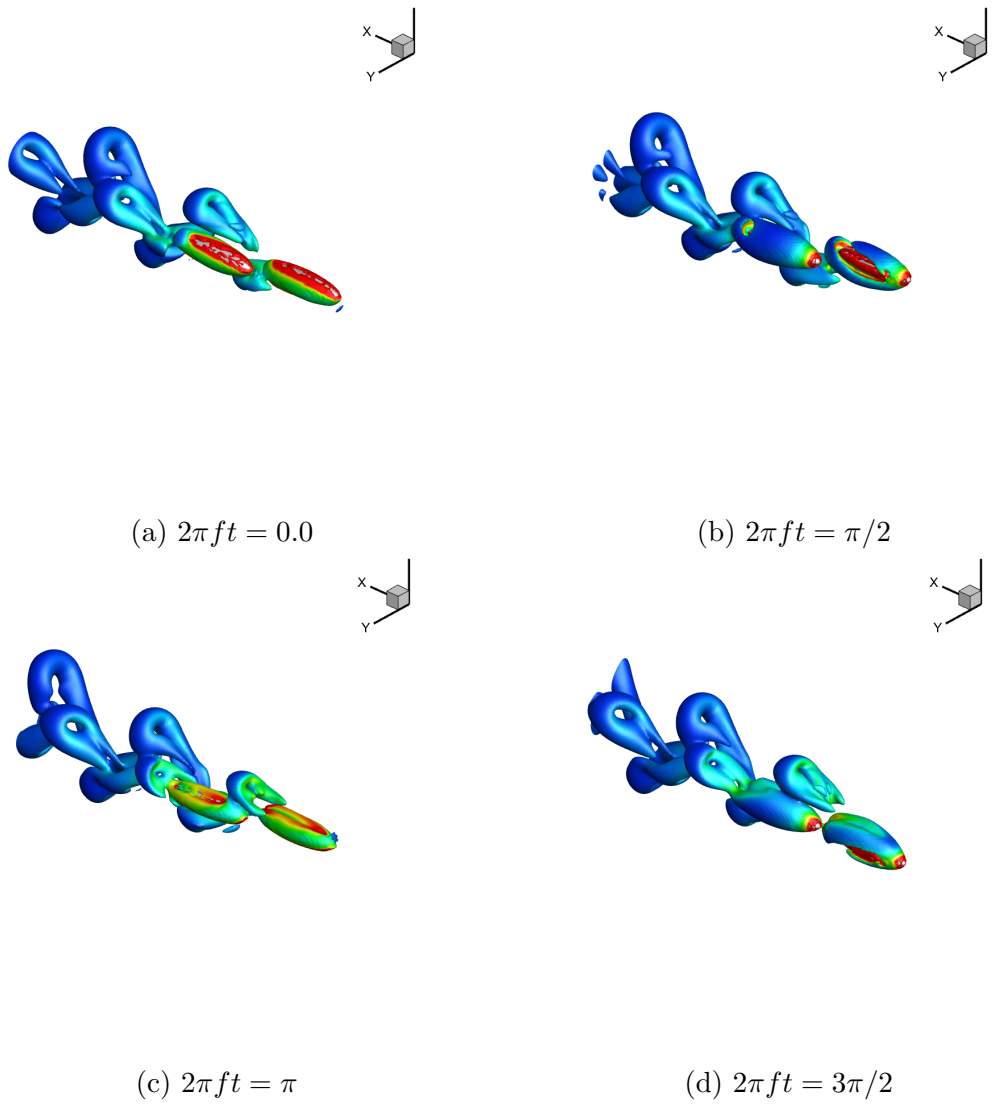

(a) $2\pi ft = 0.0$

(b) $2\pi ft = \pi/2$

(c) $2\pi ft = \pi$

(d) $2\pi ft = 3\pi/2$

Figure 3.3: Initial Conditions for Optimization. Time-lapse of fluid-structure interactions shown by vorticity magnitude, $|\omega|$, overlaid on a $+Q$-criterion iso-surface at the period intervals, $2\pi ft$, of a) 0, b) $\pi/2$, c) π, and d) $3\pi/2$.

3.3 Equal Size Optimization

In this section, an equal-sized body case is explored to maximize z-forces acting on the trailing body. The active controls for the trailing body are

$$\phi_{follow} = (A_z, A_y, \phi_z, \phi_y, z) \tag{3.4}$$

with initial and optimized values tabulated in Table 3.1. The adjoint-based optimization executed nineteen sub-iterations and five main iterations to update the gradient to a sufficient convergence shown in Fig. 3.4, (a), with no unexpected variations in iterations. Due to initial simulations converging too quickly, the error used in sub-iterations was decreased to 5×10^{-4} and main iteration allowed error to 10^{-3} and is maintained throughout the study. The history of the lift coefficient, C_L, is compared in Fig. 3.4, (b). The optimized motion whose new trajectory is shown in Fig. 3.2, (a) allows for the trailing body to enter the centerline vortex structure of the leading body. This allows for the body to be actively pushed up by the inner edges of the hairpin vortex to increase the coefficient of lift, C_L, by a relative 900% from 0.00243 to 0.2188. From a physical perspective, this specific increase can be attributed to the velocity of the rising flow underneath the leading body as it descends in the stream directly impacting the trailing body. For the period of time where the trailing body is not within the centerline vortex, it moves into the region of unperturbed flow to minimize the detrimental effects of the rising lead body.

3.4 75% Original Size Optimization

With the equal sized body case established in the previous section, this and the subsequent sections explore variations in size with respect to the trailing body. The size study cases utilize the same initial conditions, constraints, and degrees of freedom as the previous case. Fig. 3.6, (a), shows the convergence of the 75%-size case. Unlike the equal sized case, the 75% case shows a large decrease in C_L in the third main iteration. This event showcases one of the

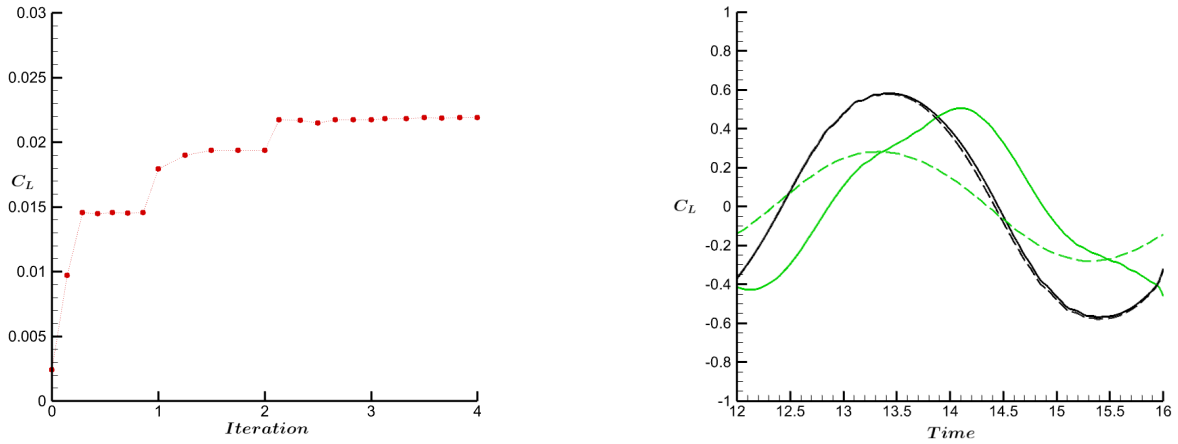

(a) (b)

Figure 3.4: Convergence and Optimization results for equal sized bodies. a) Shows the Sufficient convergence of the NLopt:COBYLA method with continuous adjoint-based gradient updates with a sub-iteration error of 5×10^{-4} and main iteration error of of 10^{-3}. b) shows the effect on the coefficient of lift, C_L, by comparing the initial conditions, lead body (- - -) and trail body (- - -), and the adjoint-based optimized results, lead body (———) and trail body (———).

limitations of the adjoint-based approach as the cost function transits between local maxima. Since the adjoint-based optimization approach is a gradient method, it is susceptible to local maxima and is dependant on initial conditions. Unlike a parametric study that maps the complete control space, which is computationally unfeasible, the adjoint-based approach optimized to a single optimized value and is thus sensitive to the initial conditions inputted. However, like the equal sized case, the 75% case also enters the centerline vortex shown by the trajectory in Fig. 3.2, (b), but due to its size is unable to maintain the optimal trailing position due to its size and movement constraints show by the C_L history in Fig. 3.6, (b), and time lapse in Fig. 3.7. As a result, the coefficient of lift, C_L, is increased from 0.00162 to 0.1260 denoting a relative 778% increase over a period of oscillation.

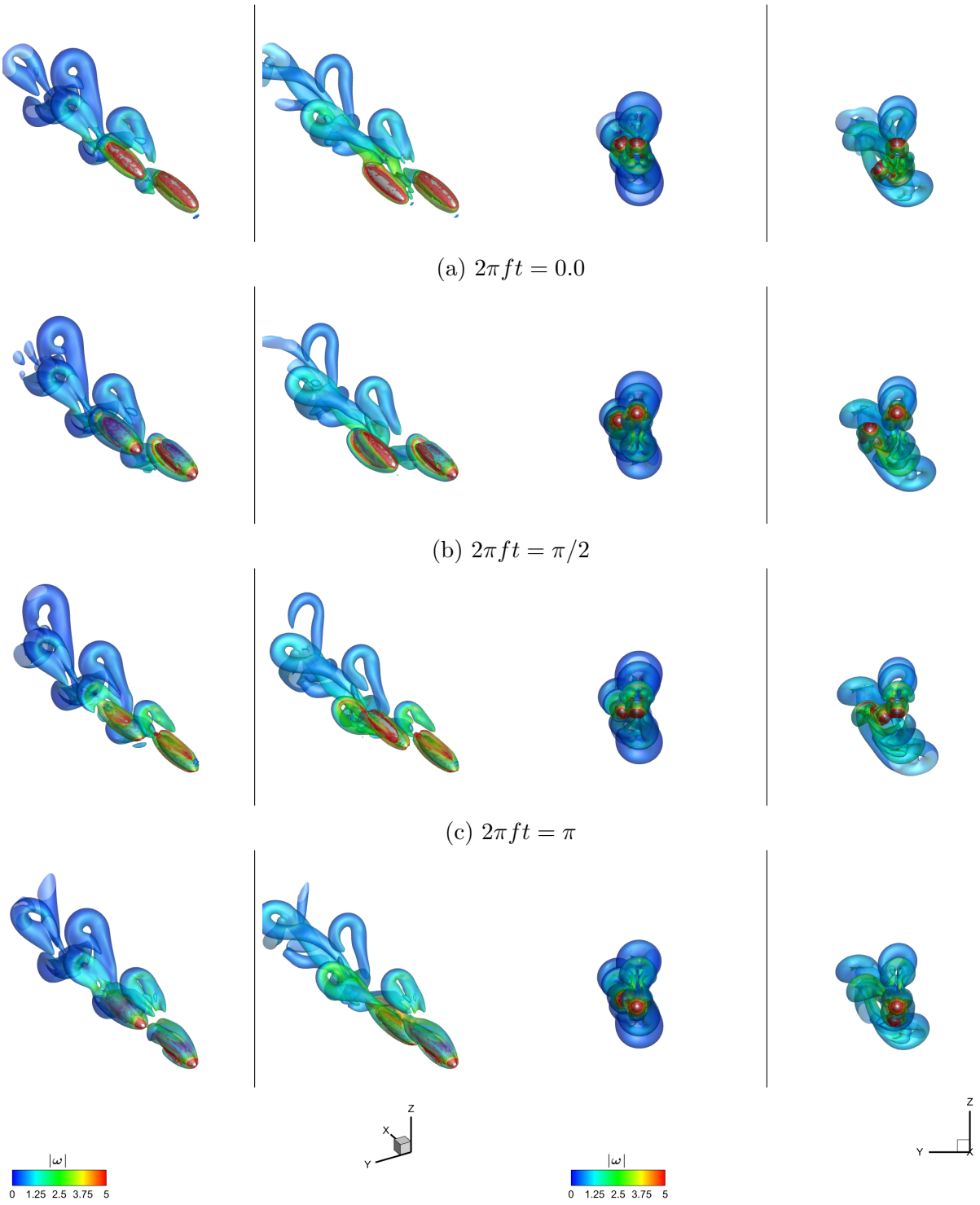

(a) $2\pi ft = 0.0$

(b) $2\pi ft = \pi/2$

(c) $2\pi ft = \pi$

(d) $2\pi ft = 3\pi/2$

Figure 3.5: Equal Size Optimization Fluid-Structure Interactions. Time-lapse of fluid-structure interactions shown by vorticity magnitude, $|\omega|$, overlaid on a $+Q$-criterion iso-surface at the period intervals, $2\pi ft$ of a) 0, b) $\pi/2$, c) π, and d) $3\pi/2$. Initial conditions are shown on the left with optimized results on the right.

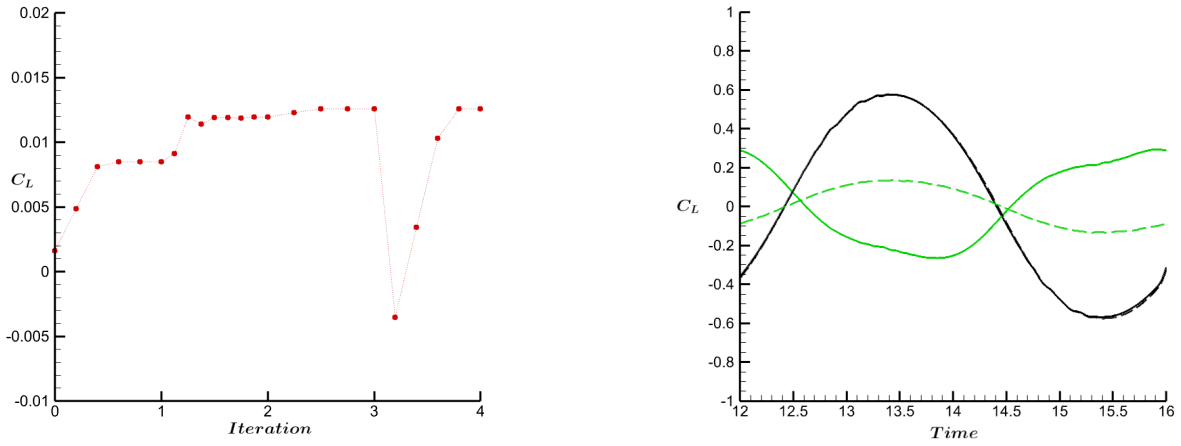

(a) (b)

Figure 3.6: Convergence and Optimization results for 75% original sized trail body. a) Shows the Sufficient convergence of the NLopt:COBYLA method with continuous adjoint-based gradient updates with a sub-iteration error of 5×10^{-4} and main iteration error of of 10^{-3}. b) shows the effect on the coefficient of lift, C_L, by comparing the initial conditions, lead body (- - -) and trail body (- - -), and the adjoint-based optimized results, lead body (———) and trail body (———).

3.5 50% Original Size Optimization

Continuing the study on the variation of size, the 50% case is the first case where the adjoint-based optimization places the trailing body outside of the centerline vortex position. In this case after sufficient, normal convergence is reached as shown in Fig. 3.8, the overall magnitude of C_L is significantly reduced. The fluid-structure time lapse in Fig. 3.9, shows the trailing body interacting with the outer wall of the leading body's hairpin vortex. During this interaction, the trailing body is able to contact positive z-directional fluid flow to increase C_L as shown in Fig. 3.8. The resulting motion results in a relative 611% increase from 0.00046 to 0.00279. However, based on the optimal values and trajectory in Fig. 3.2, (c), performance of this optimization sought to minimize the variation in magnitude of the cost function as evident by the smoothing of C_L in Fig. 3.8 despite the effects from the vortex wall interaction.

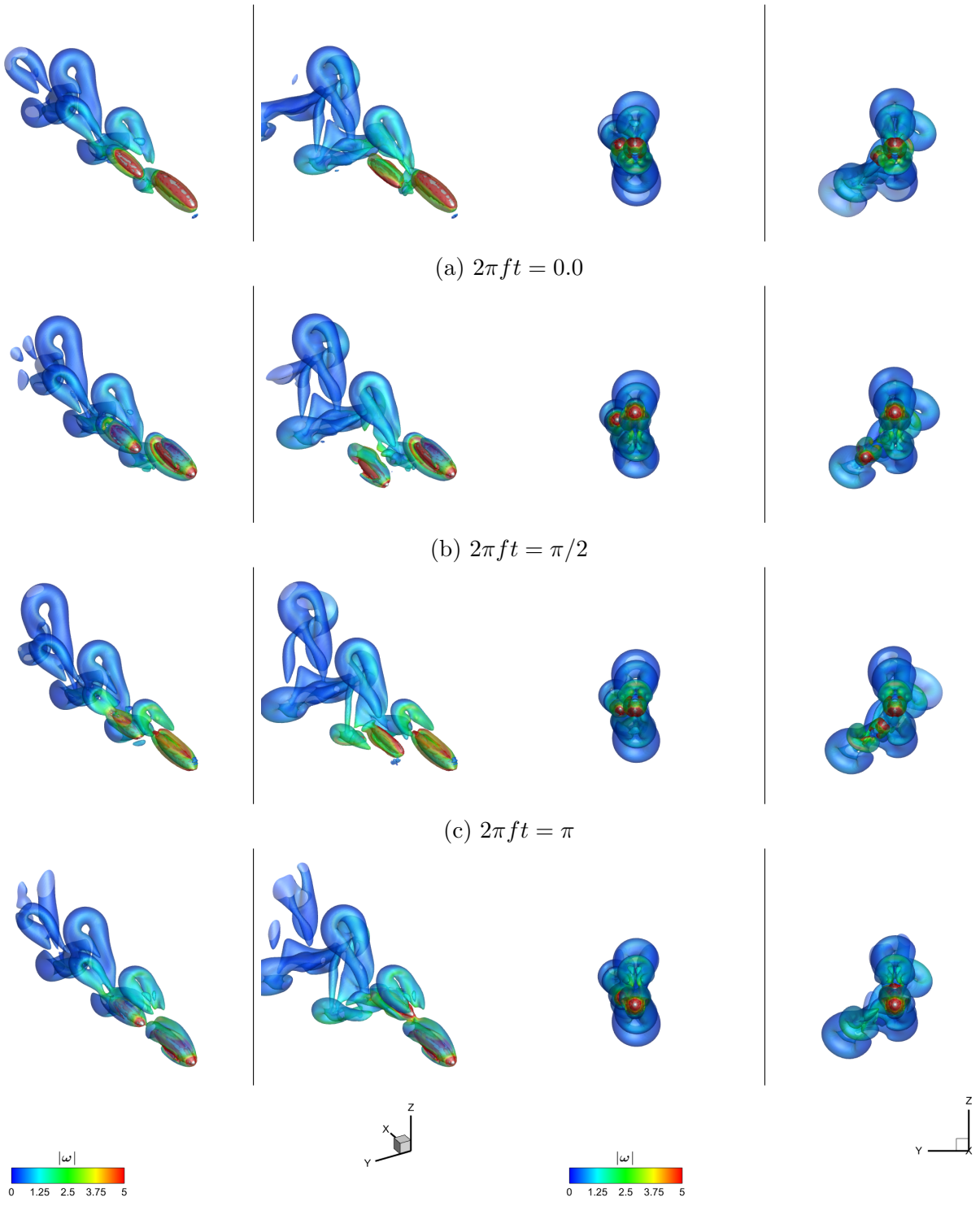

(a) $2\pi ft = 0.0$

(b) $2\pi ft = \pi/2$

(c) $2\pi ft = \pi$

(d) $2\pi ft = 3\pi/2$

Figure 3.7: 75% of Original Size Optimization Fluid-Structure Interactions. Time-lapse of fluid-structure interactions shown by vorticity magnitude, $|\omega|$, overlaid on a $+Q$-criterion iso-surface at the period intervals, $2\pi ft$, of a) 0, b) $\pi/2$, c) π, and d) $3\pi/2$. Initial conditions are shown on the left with optimized results on the right.

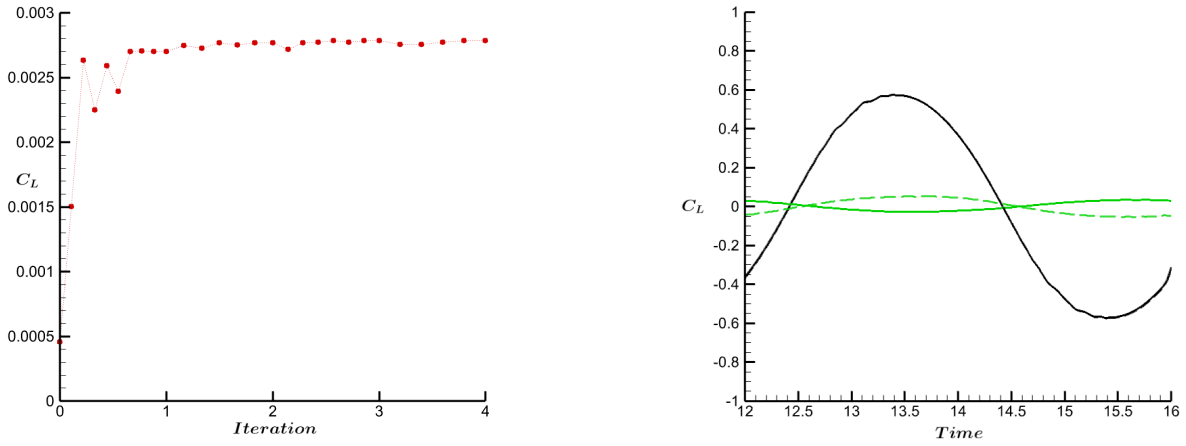

(a) (b)

Figure 3.8: Optimization results for 50% original sized trail body. a) Shows the Sufficient convergence of the NLopt:COBYLA method with continuous adjoint-based gradient updates with a sub-iteration error of 5×10^{-4} and main iteration error of of 10^{-3}. b) shows the effect on the coefficient of lift, C_L, by comparing the initial conditions, lead body (- - -) and trail body (- - -), and the adjoint-based optimized results, lead body (———) and trail body (———).

3.6 25% Original Size Optimization

The final variation in size becomes an compilation of the challenges and issues identified in the previous sections. To begin, the 25%case optimization shows the existence of local maxima in the convergence shown in Fig. 3.10 and previously discussed in the 75% case. Like the 50% case, the 25% case also travels into the outside vortex wall shown in Fig. 3.11 to achieve a more staggering 30,917% relative increase in C_L from 0.00003 to 0.00096. Although this case exhibits an abnormally large gain, this is primarily due to the near zero force experienced by the body in the free-stream flow. Due to the size of the following body in this case, it may experience additional effects not incorporated into this study such as a Bernoulli suction force often exhibited by drafting dolphins.[14]

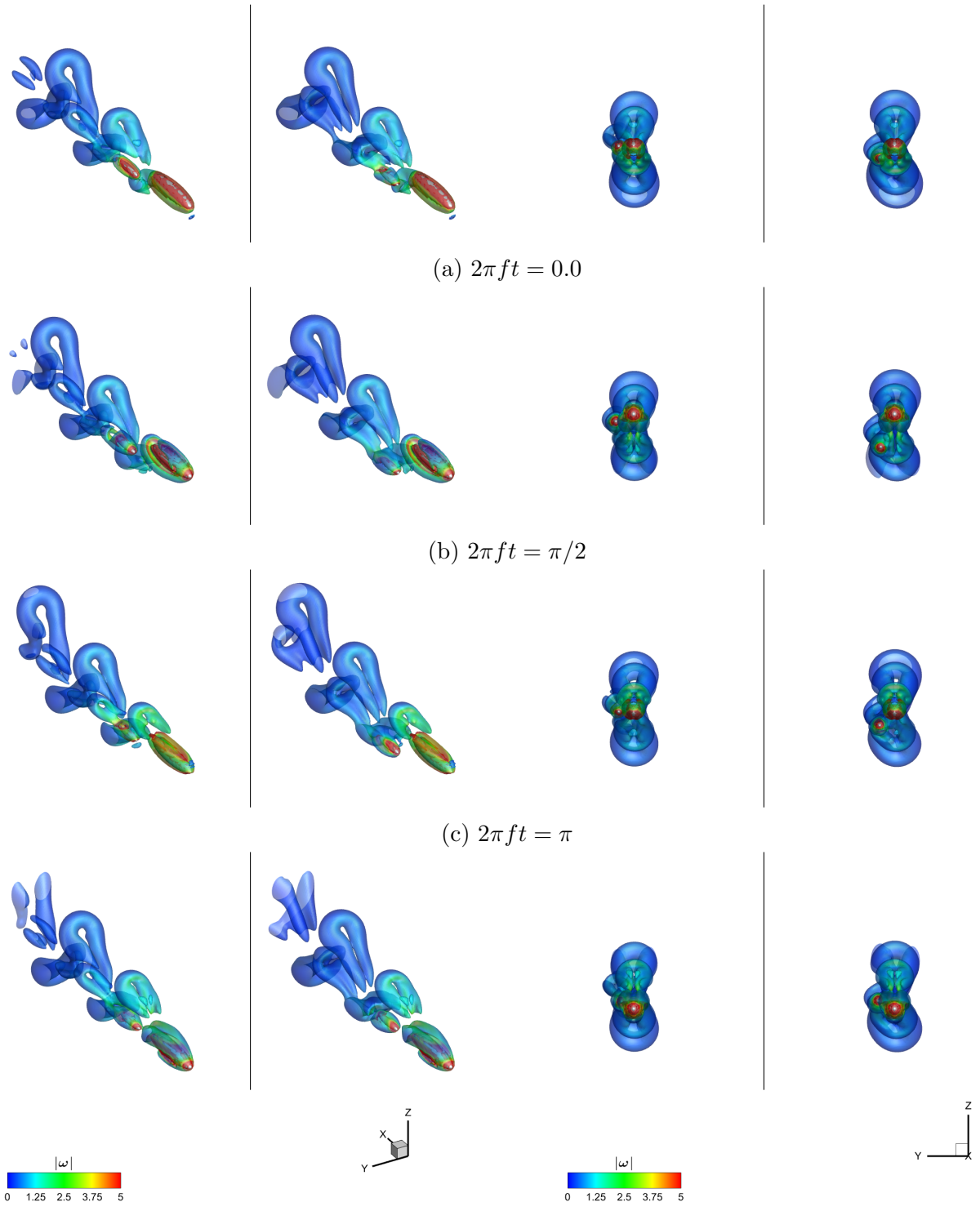

(a) $2\pi ft = 0.0$

(b) $2\pi ft = \pi/2$

(c) $2\pi ft = \pi$

(d) $2\pi ft = 3\pi/2$

Figure 3.9: 50% of Original Size Optimization Fluid-Structure Interactions. Time-lapse of fluid-structure interactions shown by vorticity magnitude, $|\omega|$, overlaid on a $+Q$-criterion iso-surface at the period intervals, $2\pi ft$, of a) 0, b) $\pi/2$, c) π, and d) $3\pi/2$. Initial conditions are shown on the left with optimized results on the right.

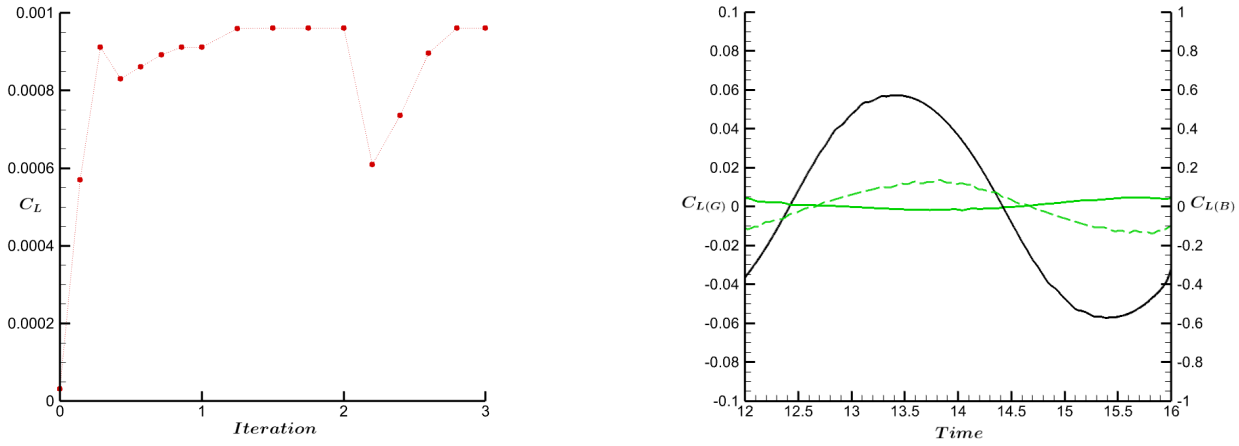

(a) (b)

Figure 3.10: Convergence and Optimization results for 25% original sized trail body. a) Shows the Sufficient convergence of the NLopt:COBYLA method with continuous adjoint-based gradient updates with a sub-iteration error of 5×10^{-4} and main iteration error of of 10^{-3}. b) shows the effect on the coefficient of lift, C_L, by comparing the initial conditions, lead body (- - -) and trail body (- - -), and the adjoint-based optimized results, lead body (———) and trail body (———).

3.7 Computational Cost of Implementation

Due to the complexity and size of the current control space, the previous cases would not be possible using traditional methods. Since the adjoint-based approach used to calculate the conjugate gradient is computationally insensitive to the number of control variables, this approach is ideal to apply to larger and more complex cases. For a standard forward simulation, the current computational time is 6.7 hours at $10,000$ iterations. A comparable parametric study, assuming five values per control parameter, has a computational cost of 2.39 years ($5^5 = 3125$ simulations). However, the above cases only required 8.1 days at the longest.

3.8 Summary of Echelon Pair Study

The cases studied in this chapter displayed some challenges and limitations of the current implementation along with identifying specific regions in the centerline position and hairpin

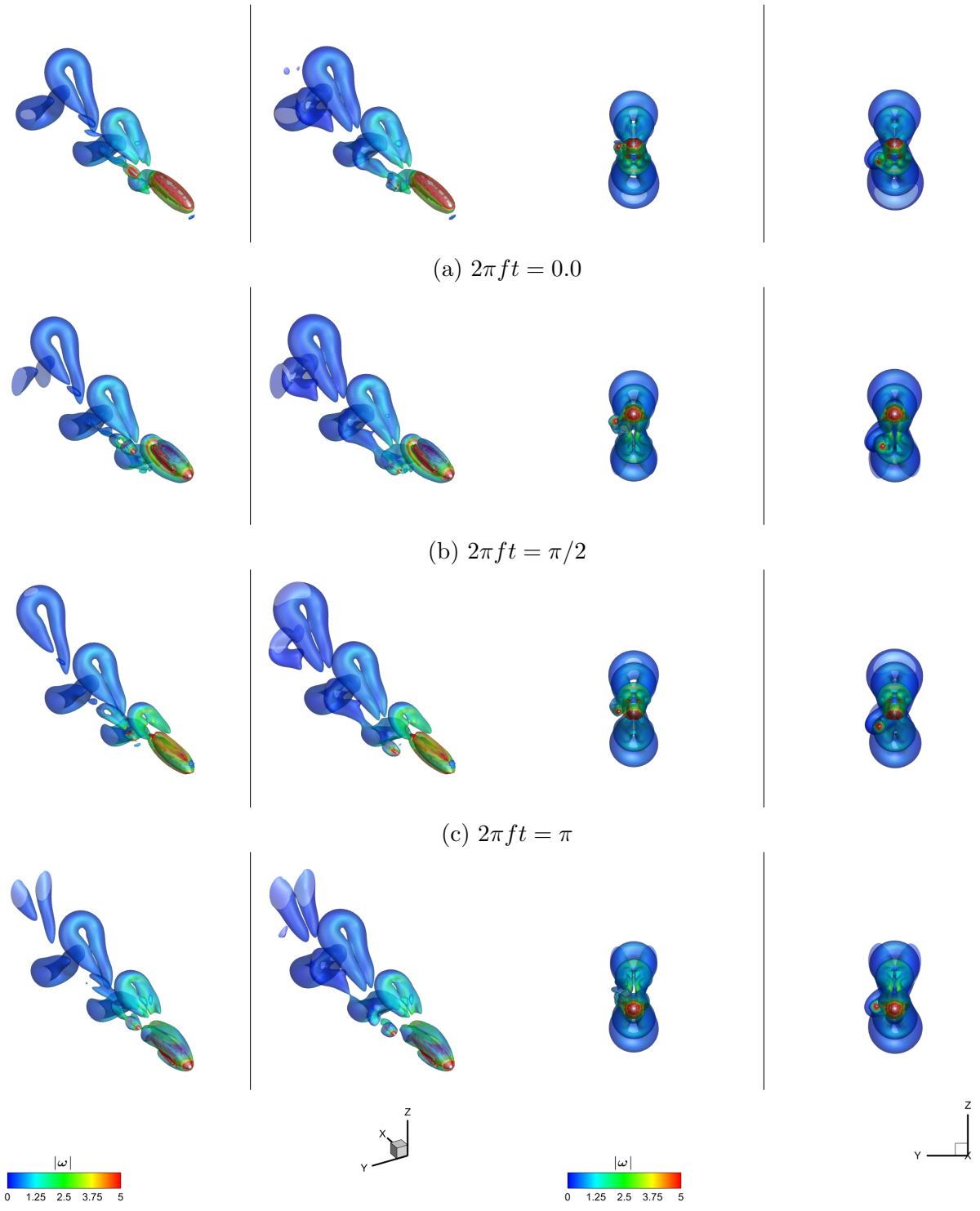

(a) $2\pi ft = 0.0$

(b) $2\pi ft = \pi/2$

(c) $2\pi ft = \pi$

(d) $2\pi ft = 3\pi/2$

Figure 3.11: 25% of Original Size Optimization Fluid-Structure Interactions. Time-lapse of fluid-structure interactions shown by vorticity magnitude, $|\omega|$, overlaid on a $+Q$-criterion iso-surface at the period intervals, $2\pi ft$, of a) 0, b) $\pi/2$, c) π, and d) $3\pi/2$. Initial conditions are shown on the left with optimized results on the right.

vortex with a beneficial influence to lifting forces for future study. The challenges facing this implementation pertain to the susceptibility of optimized solutions to become limited by a local minima or maxima. However, this susceptibility can be overcome with the future utilization of NLopt global optimization methods with local gradient-based optimization in future studies. By taking the time to study a simplistic multiple moving body scenario, the viability and validity of the application of the adjoint-based optimization approach becomes apparent for application to a larger, multiple moving body system as explored in ongoing and future work.

Chapter 4

Conclusion

Aided by non-cylindrical calculus, the adjoint-based optimization approach was expanded and applied to three-dimensional flows interacting with multiple moving bodies. By optimizing five control parameters, $\phi_{follow} = (A_z, A_y, \phi_z, \phi_y, z)$, that govern a following body's multi-directional heaving motion and relative vertical positioning, relative gains exceeding 600% were achieved. The resulting motion and variation in the trailing body sizing allowed the trailing body to beneficially interact with the leading body's wake with special emphasis the immediate centerline region and outer vortex wall of the resulting hairpin vortexes. Although the positioning of the following body was also optimized, the effect of the position gradient overpowered the effects of amplitude and stricter bounds were enforced. However, the most important conclusion from this study is the validation of the application of the adjoint-based optimization approach to three-dimensional flows interacting with multiple moving bodies. Additionally, due to the immense reduction in computational costs, larger and more complex problems are able to be studied with this approach.

Therefore, with a feasible application of the adjoint-based optimization approach to a multiple moving body system, current ongoing and future work expands the purview to the classical diamond formation undergoing pitching and heaving motions. The resulting schematic and kinematic setup is shown in Fig. 4.1. This future work strives to address additional considerations and controls required to evaluate convergence of the summation of

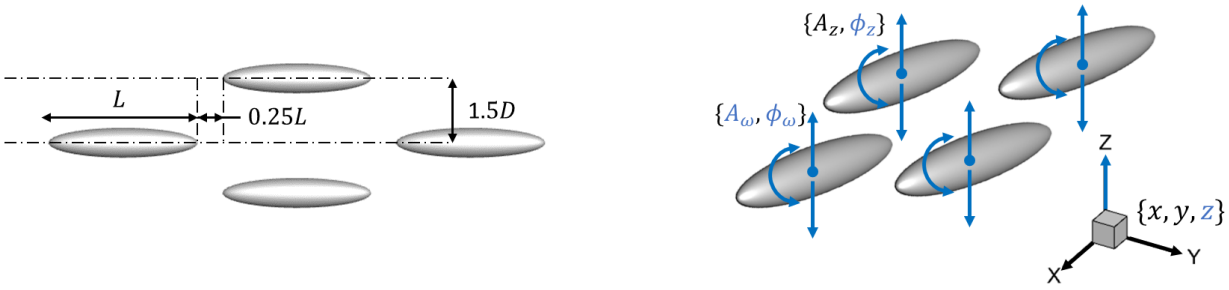

(a) (b)

Figure 4.1: Future multiple body diamond formation kinematic setup and motion decomposition. a) Schematic of the spatial positioning and layout for the study of the diamond pattern formation. b) Schematic of the decomposition of motion and active (——) and fixed (——) control parameters.

independent cost functions while optimizing more than one moving body.

Bibliography

[1] D. N. Beal, F. S. Hover, M. S. Triantafyllou, J. C. Liao, and G. V. Lauder. Passive propulsion in vortex wakes. *Journal of Fluid Mechanics*, 549, 2006.

[2] F. E. Fish. *Flow Phenomena in Nature*, chapter Diversity, mechanics and performace of natural aquatic propulsors, pages 57–86. WIT Press, 2006.

[3] J. Glynn. *Design of biomimetic passive control for optimization of oscillating hydrofoils in tidal energy capture*. PhD thesis, University of Strathclyde, 2006.

[4] H. Trenchard and P. Matjaz. Energy saving mechanisms, collective behavior and the variation range hypothesis in biological systems: a review. *BioSystems*, 147, 2016.

[5] K. Karenina, A. Giljov, V. Baranov, L. Osipova, V. Krasnova, and Y. Malashichev. Visual laterality of calf-mother interations in wild whales. *PLoS ONE*, 5(11), 2010.

[6] A. E. Nousek McGregor. *The cost of locomotion in North Atlantic right whales Eubalaena glacialis*. PhD thesis, Duke University, 2010.

[7] M. A. Smultea, D. Fertl, C. E. Bacon, M. R. Moore, V. R. James, and B. Wursig. Cetacean mother-calf behavior observed from a small aircraft off southern california. *Animal Behavior and Cognition*, 4(1), 2017.

[8] F. E. Fish, K. T. Goetz, D. J. Rugh, and L. V. Brattstrom. Hyrdrodynamic patterns associtated with echeon formation swimming by feeding bowhead whales. *Marine Mammal Science*, 29(4), 2013.

[9] L. Bejder, S. Videsen, L. Hermannsen, M. Simon, D. Hanf, and P. T. Madsen. Low energy expenditure and resting behavior of humpback whale mother-calf pairs highlights conservation importace of sheltered breeding areas. *Scientific Reports*, 9(771), 2019.

[10] S. R. de la Gala-Hernandez and G. Heckel. Comparative swimming effort of migrating gray whales (eschrichtius robustus) and calf cost of transport along costa azul, baja california, mexico. *Canadian Journal of Zoology*, 86(307), 2008.

[11] D. E. Shormann and M. Panhuis. Performance evaluation of a humpback whale-inspired hydrofoil design applied to surfboard fins. In *OCEANS 2019 MTS/IEEE Seattle*, 2019.

[12] A. P. Maertens, A. Gao, and M. S. Triantafyllou. Optimal undulatory swimming for a single fish-like body and for a pair of interacting swimmers. *Journal of Fluid Mechanics*, 813(301), 2017.

[13] X. Li, J. Gu, Z. Su, and Z. Yao. Hydrodynamic analysis of fish schools arranged in the vertical plane. *Physics of Fluids*, 33(121905), 2021.

[14] D. Weihs. The hydrodynamics of dolphin drafting. *Journal of Biology*, 3(8), 2004.

[15] S. Alben. *Natural Locomotion in Fluids and Surfaces: Swimming, Flying, and Sliding*, chapter Model problems for fish schooling, pages 3–13. Springer New York, 2012.

[16] G. Li, D. Kolomenskiy, H. Liu, B. Thiria, and R. Godoy-Diana. On the energetics and stability of a minimal fish school. *PLoS ONE*, 14(8), 2019.

[17] A. Filella, F. Nadal, C. Sire, E. Kanso, and C. Eloy. Hydrodynamic interactions influence fish collective behavior. *Phys Rev Lett*, 120(198101), 2018.

[18] S. Im, S. G. Park, Y. Cho, and H. J. Sung. Schooling behavior of rigid and flexible heaving airfoils. *International Journal of Heat and Fluid Flow*, 69, 2018.

[19] M. Gazzola, B. Hejazialhosseini, and P. Koumoutsakos. Reinforcement learning and wavelet adapted vortex methods for simulation of self-propelled swimmers. *Journal of Scientific Computing*, 36(3), 2014.

[20] D. Weihs. Semi-infinite vortex trails, and their relation to oscillating airfoils. *Journal of Fluid Mechanics*, 54(4), 1972.

[21] D. Weihs. Hydromechanics of fish schooling. *Nature*, 241, 1973.

[22] M. Daghooghi and I. Borazjani. The hydrodynamic advantages of synchronized simming in a rectangular pattern. *Bioinspiration and Biomimetics*, 10, 2015.

[23] S. G. Park and H. J. Sung. Hydrodynamics of flexible fins propelled in tandem, diagonal, triangular and diamond configurations. *Jounal of Fluid Mechanics*, 840, 2018.

[24] L. Li, M. Nagy, J. M. Graving, J. Bak-Coleman, G. Xie, and I. D. Couzin. Vortex phase matching as strategy for schooling in robors and in fish. *Nature Communications*, 11 (5408), 2020.

[25] S. Verma, G. Novati, and P. Koumoutsakos. Efficient collective swimming by harnessing vortices through deep reinforcement learning. In PNAS, editor, *Proceedings of the National Academy of Sciences of the United States of America*, volume 115, 2018.

[26] M. Xu, M. Wei, C. Li, and H. Dong. Adjoint-based optimization for thrust performance of three-diensional pitching-rolling plate. *AIAA Journal*, 57(9), 2019.

[27] M. Xu and M. Wei. Using adjoint-based approach to study flapping wings. In *51st AIAA Aerospace Sciences Meeting including the New Horizons Forum and Aerospace Exposition*, 2013.

[28] M. Xu and M. Wei. Using adjoint-based optimization to study kinematics and deformation of flapping wings. *Journal of Fluid Mechanics*, 799:56–99, 2016.

[29] M. Xu, M. Wei, C. Li, and H. Dong. Adjoint-based optimization of flapping plates hinged with a trailing-edge flap. *Theoretical and Applied Mechanics Letters*, 5(1), 2015.

[30] K. Jia, T. Scofield, M. Wei, and S. Bhattacharya. Vorticity transfer in a leading-dege vortex due to controlled spanwise bending. *Physical Review Fluids*, 6(024703), 2021.

[31] J. Reuther, A. Jameson, J. Farmer, L. Martinelli, and D. Saunders. Aerodynamic shape optimization of complex aircraft configureations via and adjoint formulation. In *34th aerospace sciences meeting ad exhibit*, 1996.

[32] T. R. Bewley, P. Moin, and R. Temam. Dns-based predictive control of turbulence: an optimal benchmark for feedback algorithms. *Journal of Fluid Mechanics*, 447, 2001.

[33] M. Wei and J. B. Freund. A noise-controlled free shear flow. *Journal of Fluid Mechanics*, 564:123–152, 2006.

[34] D. Colgan, B. Xu, M. Wei, and J. Hrynuk. 3d vortical structure of multiple moving spheroids under adjoint-based optimal control. In *AIAA SCITECH 2023 Forum*, 2023.

[35] K. Jia. *Optimization of flexible wings and vorticity transfer in a leading-edge vortex due to spanwise bending*. PhD thesis, Kansas State University, 2021.

[36] M. Xu. *Understanding flapping-wing aerodynaimcs through adjoing-based approach*. PhD thesis, New Mexico State University, 2014.

[37] C. S. Peskin. Flow patterns around heart valves: a numerical method. *Journal of Computational Physics*, 10(2):252–271, 1972.

[38] D. A. Anderson, J. C. Tannehill, R. H. Pletcher, R. Munipalli, and V. Shankar. *Computational Fluid Mechanics and Heat Transfer*. CRC Press, fourth edition, 2021.

[39] C. S. Peskin. The immersed boundary method. *Acta Numerica*, 11:479–517, 2002.

[40] R. Mittal, H. Dong, M. Bozkurttas, F. M. Najjar, A. Vargas, and A. von Loebbecke. A versatile sharp interface immersed boundary method for incompressible flows with complex boundaries. *Journal of Computational Physics*, 227(10), 2008.

[41] R. Ghias, R. Mittal, and H. Dong. A sharp interface immersed boundary method for compressible viscous flows. *Journal of Computational Physics*, 225:528–553, 2007.

[42] E. A. Fadlun, R. Verzicco, P. Orlandi, and J. Mohd-Yusof. Combined immersed-boundary finite-difference methods for three-dimensional conplex flow simulations. *Journal of Computational Physics*, 161:35–60, 2000.

[43] E. M. Saiki and S. Biringen. Numerical simulations of a cylinder in uniform flow: application of a virtual boundary method. *Journal of Computational Physics*, 123(450), 1996.

[44] M. Moubachir and J. Zolesio. *Moving Shape Analysis and Control: Applications to Fluid Structure Interactions*. Number 277 in Pure and Applied Mathematics. Chapman and Hall/CRC, 2006.

[45] B. Protas and W. Liao. Adjoint-based optimization of pdes in moving domains. *J. Comput. Phys.*, 227(4):2707–2723, 2008.

[46] S. K. Nadarajah and A. Jameson. A comparison of the continuous and discrete adjoint approach to automatic aerodynamic optimization. In *38th Aerospace Sciences Meeting and Exhibit*, page 667, 2000.

[47] S. Pirozzoli and P. Orlandi. Natural grid stretching for dns of wall-bounded flows. *Journal of Computational Physics*, 439:110408, 2021.

[48] S. G. Johnson. *The NLopt nonlinear-optimization package*, 2022.

[49] J. Zhan, Y. Li, W. Wai, and W. Hu. Comparison between the q creiteron and rortex in the application of an in-steam structure. *Physics of Fluids*, 31(121701), 2019.